

Covariant density functional theory for nuclear chirality in ^{135}Nd

J. Peng^{1,*} and Q. B. Chen^{2,†}

¹*Department of Physics, Beijing Normal University, Beijing 100875, China*

²*Physik-Department, Technische Universität München, D-85747 Garching, Germany*

The three-dimensional tilted axis cranking covariant density functional theory (3D-TAC CDFT) is used to study the chiral modes in ^{135}Nd . By modeling the motion of the nucleus in rotating mean field as the interplay between the single-particle motions of several valence particle(s) and hole(s) and the collective motion of a core-like part, a classical Routhian is extracted. This classical Routhian gives qualitative agreement with the 3D-TAC CDFT result for the critical frequency corresponding to the transition from planar to aplanar rotation. Based on this investigation a possible understanding of tilted rotation appearing in a microscopic theory is provided.

PACS numbers: 21.10.Re, 21.60.Jz, 21.10.Pc, 27.60.+j

Triaxial nucleus, shaped like a kiwi with all three principal axes unequal, has drawn considerable attention over the years. While being rare in the ground state [1], it becomes more common at high spin [2]. For high spin, the orientation of angular momentum vector relative to the triaxially deformed density distribution becomes a very important concept [3]. The angular momentum may align along one of principal axes (principal axis rotation), lie in one of the principal planes defined by two principal axes (planar rotation), and deviate from the principal planes (aplanar rotation). Note that the second and the third motions are also called as tilted rotation.

For tilted rotation, its physical interpretation was given in Ref. [4] by studying the model system of one $h_{11/2}$ particle and one $h_{11/2}$ hole coupled to a triaxial rotor with the irrotational flow type of moments of inertia (MoIs). In detail, the high- j particle/hole tends to align along the short/long (s -/ l -) axis because its torus-like/dumbbell-like density distribution has the maximal overlap with the triaxial core in the medium-long/medium-short (ml -/ ms -) plane. The triaxial rotor tends to align along the medium (m -) axis since it is of the largest MoI. As a consequence, the total angular momentum will firstly lie in the sl -plane and with increasing spin be tilted towards the m -axis, i.e., showing a transition from planar to aplanar rotation.

The occurrence of aplanar rotation manifests itself as the observation of a pair of nearly degenerated $\Delta I = 1$ bands with the same parity in the laboratory. They are called as chiral doublet bands [4], since in the aplanar rotation the mutually perpendicular angular momenta of the valence particle, valence hole, and rotor can be arranged to form two systems which differ by chirality, i.e., a left- and a right-handed system. Correspondingly, the excitation modes based on the aforementioned planar and aplanar rotations are called as chiral vibration and chiral rotation, respectively.

As is well-known, the chirality is a phenomenon existing commonly in nature, such as, the spiral arm of the nebula, the spirals of snail shells, and the handedness of amino acids. Therefore, the propose [4] and observation [5] of chirality at nuclear high spin state caused quite a stir among nuclear struc-

ture physics [61], and has intrigued lots of investigations from both theoretical and experimental aspects. Up to now, more than 50 chiral nucleus candidates spread in the mass regions of $A \sim 80, 100, 130, \text{ and } 190$ have been reported, see, e.g., data tables [6].

As mentioned above, the nuclear chirality was proposed based on the study of angular momentum vector geometry of a phenomenological model system with a particle and a hole coupled to a triaxial rotor [4]. This model system reveals the duality of the single-particle and collective properties of atomic nuclei and has been used extensively in the development of (triaxial) particle rotor model (PRM) [7, 8]. By the newly developed many-particle-many-hole PRM (e.g., Refs. [9–19]), the understanding of the nuclear chirality is deeply entrenched.

To verify the prediction by the model system, microscopic three-dimensional tilted axis cranking (3D-TAC) calculations in a hybrid Woods-Saxon and Nilsson model combined with the shell correction method were carried out [20]. In the 3D-TAC calculation, with the mean field approximation for the two body interaction, all of the nucleons are treated on the same footing. It allows also for an arbitrary orientation of the angular momentum vector in the intrinsic frame. The solution for each rotational frequency ω is obtained self-consistently by minimizing the total Routhian surface, which is the energy surface of the rotating nucleus in the intrinsic frame, with respect to the orientation of angular velocity vector $\omega = \omega(\sin \theta \cos \varphi, \sin \theta \sin \varphi, \cos \theta)$. Here, usually, θ is the polar angle between the ω and l -axis, and φ is the azimuthal angle between the projection of ω onto the ms -plane and the s -axis. The authors of Ref. [20] found that when cranking a realistic system with triaxially deformation and high- j particle-hole configuration, $\theta \neq 0, \pm\pi/2, \varphi = 0, \pm\pi/2$ for planar rotation at low ω , and $\theta \neq 0, \pm\pi/2, \varphi \neq 0, \pm\pi/2$ for aplanar rotation above a certain value of ω (denoted as ω_{crit}).

Subsequently, an analytical formula of ω_{crit} , called as the critical frequency, was derived in Ref. [21]. In the derivation, using the aforementioned model system, the particle and hole are further assumed to align rigidly along the s - and l -axis, respectively. Further self-consistent calculations by the 3D-TAC Skyrme-Hartree-Fock method show that ω_{crit} depends on the effective interaction used [21, 22]. Very recently, 3D-TAC calculations based on covariant density functional theory (3D-

*Electronic address: jpeng@bnu.edu.cn

†Electronic address: qbchen@pku.edu.cn

TAC CDFT) [23] also support the existence of ω_{crit} .

In the 3D-TAC calculations, the model system that valence nucleons coupled to a triaxial rotor is not necessary to be assumed a priori, since all of the nucleons are treated on the same footing in the rotating mean field. Then a straightforward question comes: which part of nucleon(s) drives the total nuclear system to exhibit an aplanar rotation? Inspired by the entrenched picture in model system, we might wonder whether there exists really a hidden collective core-like part and this “core” plays a role driving the rotational axis toward to the m -axis to stimulate the aplanar rotation. In this work, we try to figure out this core-like part and based on it provide a possible understanding of tilted rotation appearing in the microscopic 3D-TAC calculations.

As an example, the chiral modes in nucleus ^{135}Nd will be studied. The reasons for studying ^{135}Nd are as follows. Experimentally, this nucleus is a possible candidate nucleus with multiple chiral doublet ($M\chi D$) phenomenon [24, 25] as two pairs of chiral doublet bands were reported. One of them (labeled as bands D5 and D6 in the current work), built on the configuration $\pi h_{11/2}^2 \otimes \nu h_{11/2}^{-1}$ (labeled as config2), is the first reported chiral doublet bands of odd- A nuclei [26] and with rare lifetime measurement results [27]. The other one (labeled as bands D3 and D4), built on the configuration $\pi [h_{11/2}^1(gd)^1] \otimes \nu h_{11/2}^{-1}$ (labeled as config1), is just established very recently [28]. Theoretically, ^{135}Nd has drawn attentions from various different kinds of models, such as the microscopic 3D-TAC model based on hybrid of Woods-Saxon and Nilsson potential combined with the shell correction method [26] and the 2D-TAC CDFT [29], the beyond cranking mean field random phase approximation (RPA) [27], the algebraic interacting boson-fermion model (IBFM) [30], and the phenomenological PRM [12, 28]. Therefore, the study of ^{135}Nd is a matter of general interest and has double meaning of experimental and theoretical aspects. In this work, the 3D-TAC CDFT will be further used to study the chirality in this nucleus.

The covariant density functional theory (DFT) based on the mean field approach has played an important role in a fully microscopic and universal description of a large number of nuclear phenomena [31–35]. In order to describe nuclear rotation, covariant DFT has been extended with the cranking mode [23, 36–39]. Using these extended cranking covariant DFT, lots of rotational excited states has been described well, such as superdeformed bands [36], magnetic [37–41] and anti-magnetic rotations [42–45], etc. For chirality in nuclei, $M\chi D$ phenomenon has been suggested and investigated based on constrained triaxial covariant DFT calculations [24, 46–51]. In particular, the newly developed three-dimensional tilted axis cranking (3D-TAC) covariant DFT has been successfully applied for the chirality in ^{106}Rh [23], ^{136}Nd [52] and ^{106}Ag [53].

Our microscopic calculations are performed using 3D-TAC CDFT [23, 53] with the effective point-coupling interaction PC-PK1 [54], and a three-dimensional Cartesian harmonic oscillator basis with ten major shells are used to solve the Dirac equation. The pairing correlation is neglected in the current investigation, but one has to bear in mind it could have some influences on the critical frequency [21] and the descriptions

of total angular momentum and $B(M1)$ values [29].

As mentioned above, in 3D-TAC calculations, the orientation of the angular velocity ω with respect to the three principal axes (θ, φ) is determined in a self-consistent way by minimizing the total Routhian. In these minima with $(\theta_{\text{min}}, \varphi_{\text{min}})$, the deformation parameters (β, γ) are about $(0.23, 21^\circ)$ for config1 and $(0.24, 22^\circ)$ for config2, respectively. They change within $\Delta\beta = 0.02$ and $\Delta\gamma = 3^\circ$, exhibiting a stability with the rotation. The θ_{min} varies from 50° to 68° for config1 and from 63° to 66° for config2 driven by rotation.

Since the sign of φ can be used to characterize the chirality of the rotating system [55], here we can only focus on how does the total Routhian behave with φ . By minimizing the total Routhians with respect to θ for given φ , the total Routhian curves are shown in Fig. 1 for two configurations at several typical rotational frequencies. One can see that all the curves are, analogy to the schematic picture of left- and right-hand, symmetrical with the $\varphi = 0$ line. This means that the two chiral configurations with $\pm|\varphi|$ for a given θ are identical on the energy.

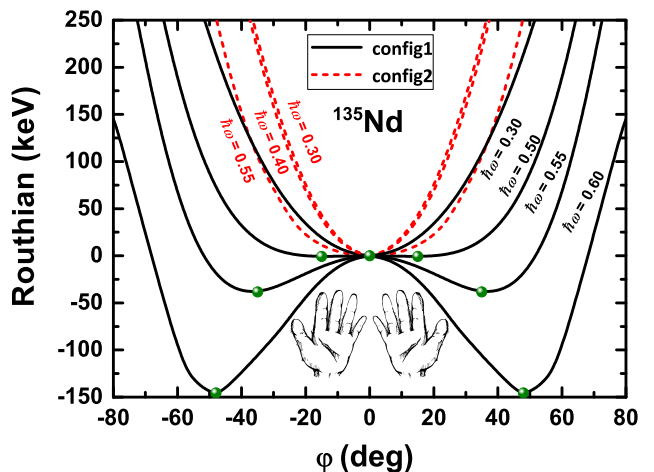


FIG. 1: Total Routhian curves as functions of the azimuth angle φ calculated by 3D-TAC CDFT for configurations $\pi [h_{11/2}^1(gd)^1] \otimes \nu h_{11/2}^{-1}$ (config1) and $\pi h_{11/2}^2 \otimes \nu h_{11/2}^{-1}$ (config2) in ^{135}Nd . All curves are normalized at $\varphi = 0$. The minima of the curves are denoted by the balls.

For both configurations, the Routhian curves are rather steep at low ω , and become softer with respect to φ with increasing ω . The $\varphi_{\text{min}} = 0$ corresponds to a planar rotation in the sl -plane for the yrast band. At slightly larger energy, the angular momentum J in fact could, according to the beyond TAC mean field approximation investigations [27, 55–57], execute harmonic oscillation with respect to the sl -plane and enter into the left- and right- sector back and forth. This motion, generating the yrare band, is called as chiral vibration [5].

For config1, there appears two degenerate minima ($|\varphi_{\text{min}}| \sim 15^\circ$) on the Routhian curve at $\hbar\omega = 0.50$ MeV. However, the curve is rather flat in the region $-20^\circ \leq \varphi \leq 20^\circ$. For higher $\hbar\omega$, the barrier of the Routhian at $\varphi = 0$ increases rapidly. The height of the barrier goes up to ~ 150 keV at $\hbar\omega = 0.60$ MeV. The higher and wider barrier of the Routhian will suppress more the tunnelings between the left- and right-handed

configurations and lead to a stronger degeneracy of the chiral doublet bands [55]. This is in qualitative agreement with the experimental observation of the closer of the bands D3 and D4 shown later in Fig. 4(a).

For config2, unfortunately, the calculations could not be followed successfully up to the largest observed spin $23.5\hbar$. Convergent results of configuration-fixed calculations could be attained only up to $\hbar\omega = 0.55$ MeV, corresponding to $I \sim 21\hbar$. By further increasing ω , a level crossing between the neutron $h_{11/2}$ and $h_{9/2}$ orbits appears. This leads to a new configuration $\pi h_{11/2}^2 \otimes \nu h_{9/2}^1$. Therefore, it might imply that the ω_{crit} for config2 in the present 3D-TAC CDFT calculation is larger than $\hbar\omega = 0.55$ MeV. For comparison, the ω_{crit} is $\hbar\omega = 0.50$ MeV in the 3D TAC calculation based on hybrid of Woods-Saxon and Nilsson potential combined with the shell correction method in Ref. [26].

The rotational motion of triaxial nuclei attains a chiral character if the angular momentum has substantial projections on all three principal axes of the triaxially deformed nucleus [4]. In a microscopic picture, the angular momentum comes from the individual nucleons in a self-consistent calculation. In order to check the mechanism behind the generation of the angular momentum, it is important to extract the contributions of the individual nucleons to the angular momentum. The results from 3D-TAC CDFT for config1 at the minima of the Routhian are presented as an example in Fig. 2.

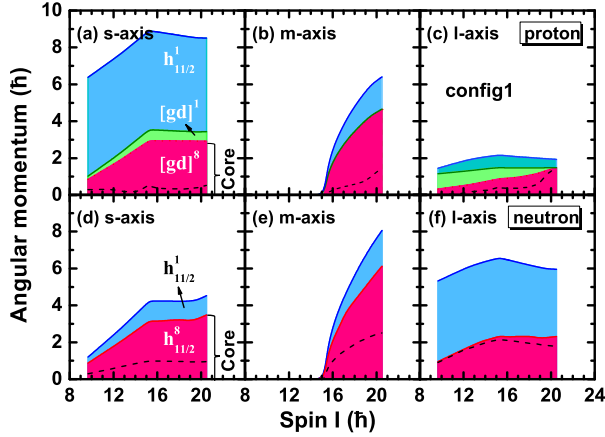


FIG. 2: Contributions of the valence protons and neutrons in the $h_{11/2}$ and (gd) shells as well as the residual core-like part to the total proton and neutron angular momenta along the s -, m -, and l -axis for config1 in ^{135}Nd .

One observes that the contribution to the proton angular momenta along the s -axis originates mainly from the high- j orbit, i.e., a proton filling at the bottom of $h_{11/2}$ orbit. The valence proton occupying in the (gd) shell orbit contributions quite small along the three principal axes ($< 1\hbar$). In contrast, a neutron sitting at the third $h_{11/2}$ shell from the top downward contributes an angular momentum of roughly $4.5\hbar$ along the l -axis. When the rotational frequency increases, the contributions of the valence protons and neutron change barely along the s - and l -axis, respectively.

The equivalent core composed from the remaining nucle-

ons now can be separated as two parts, i.e., proton and neutron parts. In more detail, the eight protons/neutrons in the $(gd)/h_{11/2}$ shell contribute to the s -axis component, and the other nucleons make main contributions on the l -axis component. Both proton and neutron parts contribute together to the m -axis component after the ω_{crit} .

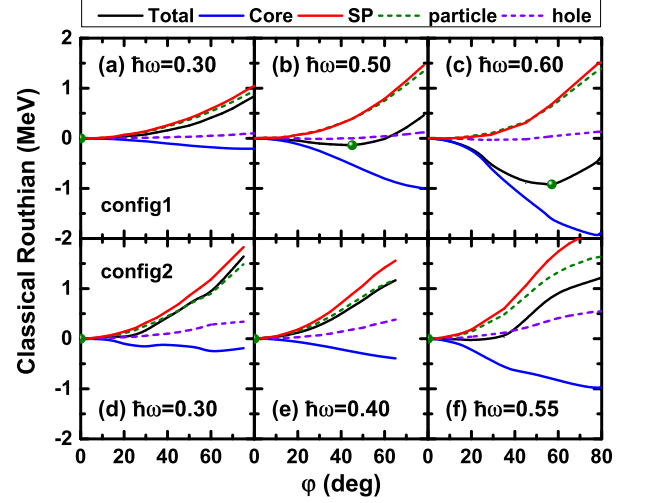


FIG. 3: Classical Routhians as functions of φ for the total, core as well as the valence particle(s), valence hole(s), and their summation (SP). All curves are normalized at $\varphi = 0$. The minimum of the total Routhian is denoted by the ball.

Adopted the same ideas in Refs. [4, 58, 59], the model study separates the nucleus into several valence nucleons and a collective core-like part. Correspondingly, the total classical Routhian of the nucleus is calculated as

$$E'_{\text{Total}} = E'_{\text{SP}} + E'_{\text{core}} = \sum_{i=\text{p,h}} \epsilon'_i - \frac{1}{2} \sum_{k=s,m,l} \mathcal{J}_k \omega_k^2, \quad (1)$$

in which the first term $\epsilon'_{\text{p,h}}$ is the single-particle Routhian for the valence particle(s) and hole(s), and the second term the Routhian for the core-like part. Inspired by this expression, we make an attempt on understanding the appearance of tilted rotation shown in Fig. 1. Starting from 3D-TAC CDFT results, we extract, intuitively, the values of $\epsilon'_{\text{p,h}}$ in Eq. (1) from the obtained single-particle Routhian for those valence particle(s) and hole(s) that the configuration information gives. As a consequence, the “core” is composed by the remaining nucleons. Its angular momentum R_k^{core} is thus the summation of these remaining nucleons’ angular momentum. Correspondingly, its MoIs can be extracted as $\mathcal{J}_k = R_k^{\text{core}}/\omega_k$, and finally its Routhian E'_{core} is yielded by Eq. (1). The obtained results of these classical Routhians as functions of φ are shown in Fig. 3.

It is observed that the values of $\epsilon'_{\text{p,h}}$ and E'_{core} increase and decrease with φ , respectively. The former indicates the valence particle(s) and hole(s) prefer to the sl -plane, and the latter represents that the core-like part favors the m -axis. Their competitions determine the rotational orientation of the total system. These features are consistent with previous model studies [4].

For config1, after $\hbar\omega = 0.50$ MeV, the steeper variation behavior of E'_{core} than those of E'_{SP} provides stronger Coriolis force and drives rotational axis deviating from the s - l plane to minimize the energy. The minima of total classical Routhian thus shift from zero to nonzero, which corresponds to the aplanar solution, in line with the results shown in Fig. 1 though the detailed value of φ_{min} and the height of the barrier are different. Therefore, a transition from planar to aplanar rotation has been displayed for config1.

For config2, the increments in E'_{SP} are larger than the decrement in E'_{core} . This is mainly caused by the two aligned $h_{11/2}$ particles, which has a very large alignment along the s -axis and make their Routhians become very steep with the increase of φ . The minimum of total classical Routhian stays at $\varphi_{\text{min}} = 0$, which corresponds to the planar regime. This is also agreement with the microscopic results shown in Fig. 1.

In the previous model studies [4, 12, 15, 16, 28], the transition from planar to aplanar rotation is attributed to the MoI of the m -axis, with the assumption of irrotational flow type $\mathcal{J}_k^{\text{irr}} \propto \sin^2(\gamma - 2k\pi/3)$, is the largest. In this work, the three MoIs for the core-like part are extracted as $\mathcal{J}_k = R_k^{\text{core}}/\omega_k$ ($k = s, m, l$) from the 3D-TAC CDFT results. We find that \mathcal{J}_k does not change much with the increase of ω and φ . In addition, \mathcal{J}_m is indeed the largest for both configurations. In detail, e.g., at $\hbar\omega = 0.30$ MeV, the ratio of $\mathcal{J}_m : \mathcal{J}_s : \mathcal{J}_l$ at $\varphi = 0$ is about 1.00 : 0.65 : 0.50 for config1 and 1.00 : 0.78 : 0.76 for config2, respectively. This feature is consistent with those empirical MoI values extracted from the 2_2^+ states in even-even nuclei [60] and supports the assumption of $\mathcal{J}_k^{\text{irr}}$ in the model study. In Ref. [21] the MoIs are extracted for the whole system from the 3D-TAC Skyrme-Hartree-Fock calculations, and the m -axis one is the largest as well. Furthermore, one notes that the ratios of $\mathcal{J}_s(\mathcal{J}_l) : \mathcal{J}_m$ for config2 is larger than that for config1. This makes, according to the formula of ω_{crit} in Ref. [21], the planar rotation become more stable, and the aplanar rotation is not easy to be obtained as shown in Fig. 1.

Therefore, we can possibly understand how dose the titled rotation occur in the 3D-TAC calculations. Though moving in the same rotating mean field, some (unpaired) valence high- j nucleons are active with significant single-particle motion and act as valence particle(s) or hole(s), while the (paired) others are not that active but exhibit collective behavior and form a stable core-like part. This core-like part has finite MoIs along the three principal axis (as indication of triaxial deformation), and the m -axis one is the largest. At low ω , the collective core angular momentum is small and is driven to lie in the sl -plane by the strong Coriolis forces from the valence particle(s) and hole(s). With increasing ω , the gradual increasing core angular momentum along the m -axis becomes comparable to those of valence particle(s) and hole(s) along s - and l -axis and results in the transition from planar to aplanar rotation.

With the above studies, the comparisons between the 3D-TAC CDFT results and the available experimental data [26–28] are given in Fig. 4.

As the calculations are carried out without additional adjustable parameters and the theoretical bandhead energies of both configurations are shifted by the same value, the qualities of present reproduction are reasonable for energy spectra. In

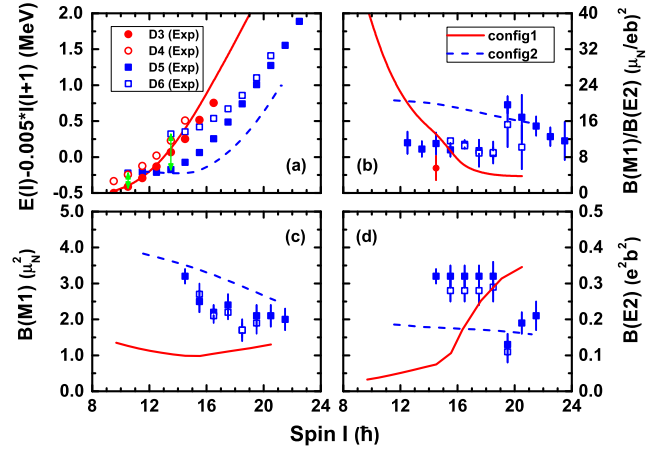


FIG. 4: Calculated results by 3D-TAC CDFT in comparisons with the available data [26–28] of doublet bands D3 and D4 and bands D5 and D6 in ^{135}Nd : (a) energies minus a common rotor contribution, (b) $B(M1)/B(E2)$ ratios, (c) $B(M1)$, and (d) $B(E2)$. The double pointed arrows between the experimental doublet bands in (a) indicate their energy differences.

addition, the larger experimental energy differences between bands D6 and D5 than bands D4 and D3 at low spin region correlate with their steeper behavior of Routhian as observed in Figs. 1 and 3.

The calculated $B(M1)/B(E2)$ values of config1 show a steep falling behavior in the planar rotation regime, and the falling tendency slows down after the transition to aplanar rotation. There is only one experimental value of $B(M1)/B(E2)$ at $I = 14.5\hbar$ for band D3 [28], which is slightly smaller than those of config1. For band D5, one observes that the calculated result with config2 shows a good agreement with the data within the error bar after $I = 18.5\hbar$. However, it overestimates the data in the lower spin region. It is caused by, as shown later, underestimating the $B(E2)$ values from $I = 14.5$ to $18.5\hbar$.

For $B(M1)$, results of config2 are in reasonable agreement with the available data of band D5. They show a smooth decreasing tendency with spin. The config1, as less of a high- j $h_{11/2}$ particle than config2, gives smaller $B(M1)$ values. However, it also shows a decreasing trend in the planar rotation region. In the aplanar region, it increases a bit.

The $B(E2)$ value depends on the deformation parameters and the orientation angles θ_{min} and φ_{min} . As the deformation and θ_{min} change slightly in config2, the calculated $B(E2)$ values are roughly constant, in line with the behavior of the experimental value. However, the calculated values of $B(E2)$ are somewhat smaller than the observed values. As shown in Ref. [29], the including of pairing correlations could improve a bit this agreement. For config1, the calculated $B(E2)$ values increase slowly for planar rotation while rapidly for aplanar rotation. This implies that, as shown in Figs. 2 and 3, the collective core-like part plays more and more important role with the increase of spin. Thus further experimental efforts in particular the lifetime measurement to extract $B(M1)$ and $B(E2)$ values, are encouraged for the bands D3 and D4.

In summary, the 3D-TAC CDFT is used to study the chiral modes in ^{135}Nd . The transition from planar to aplanar rotation is found for config 1 of band D3, while only the planar rotation for config 2 of band D5. By modeling the motion of the nucleus in rotating mean field as the interplay between the single-particle motion of several valence particle(s) and hole(s) and the collective motion of a core-like part, a classical Routhian is extracted. This classical Routhian gives qualitative agreement with the 3D-TAC CDFT result of the critical frequency for the transition from to aplanar rotation. In addition, the extracted MoIs of the core-like part has the largest value along the m -axis. Based on this investigation a possible understanding of tilted rotation appearing in a microscopic theory is provided. Current study also indicates the effects of core-like part indeed exists in the realistic rotating nucleus and thus provides a justification for the assumptions

of the phenomenological model, and more importantly reinforces the duality of single-particle and collective properties in atomic nuclei.

Acknowledgments

The authors thank P. W. Zhao for providing the numerical code of 3D-TAC CDFT. This work is supported by the National Natural Science Foundation of China (NSFC) under Grants No. 11775026 and 11875027, and the Deutsche Forschungsgemeinschaft (DFG) and NSFC through funds provided to the Sino-German CRC110 ‘‘Symmetries and the Emergence of Structure in QCD’’ (DFG Grant No. TRR110 and NSFC Grant No. 11621131001).

-
- [1] P. Möller, R. Bengtsson, B. G. Carlsson, P. Olivius, and T. Ichikawa, *Phys. Rev. Lett.* **97**, 162502 (2006).
- [2] T. R. Werner and J. Dudek, *At. Data Nucl. Data Tables* **59**, 1 (1995).
- [3] S. Frauendorf, *Rev. Mod. Phys.* **73**, 463 (2001).
- [4] S. Frauendorf and J. Meng, *Nucl. Phys. A* **617**, 131 (1997).
- [5] K. Starosta, T. Koike, C. J. Chiara, D. B. Fossan, D. R. LaFosse, A. A. Hecht, C. W. Beausang, M. A. Caprio, J. R. Cooper, R. Krücken, et al., *Phys. Rev. Lett.* **86**, 971 (2001).
- [6] B. W. Xiong and Y. Y. Wang, *Atom. Data Nucl. Data Tables* **125**, 193 (2019).
- [7] A. Bohr, *Rev. Mod. Phys.* **48**, 365 (1976).
- [8] A. Bohr and B. R. Mottelson, *Nuclear structure*, vol. II (Benjamin, New York, 1975).
- [9] J. Peng, J. Meng, and S. Q. Zhang, *Phys. Rev. C* **68**, 044324 (2003).
- [10] T. Koike, K. Starosta, and I. Hamamoto, *Phys. Rev. Lett.* **93**, 172502 (2004).
- [11] S. Q. Zhang, B. Qi, S. Y. Wang, and J. Meng, *Phys. Rev. C* **75**, 044307 (2007).
- [12] B. Qi, S. Q. Zhang, J. Meng, S. Y. Wang, and S. Frauendorf, *Phys. Lett. B* **675**, 175 (2009).
- [13] E. A. Lawrie and O. Shirinda, *Phys. Lett. B* **689**, 66 (2010).
- [14] K. Starosta and T. Koike, *Phys. Scr.* **92**, 093002 (2017).
- [15] Q. B. Chen, B. F. Lv, C. M. Petrache, and J. Meng, *Phys. Lett. B* **782**, 744 (2018).
- [16] Q. B. Chen, N. Kaiser, U.-G. Meißner, and J. Meng, *Phys. Rev. C* **99**, 064326 (2019).
- [17] Y. Y. Wang, S. Q. Zhang, P. W. Zhao, and J. Meng, *Phys. Lett. B* **792**, 454 (2019).
- [18] J. Peng and Q. B. Chen, *Phys. Lett. B* **793**, 303 (2019).
- [19] J. Peng and Q. B. Chen, *Phys. Lett. B* **806**, 135489 (2020).
- [20] V. I. Dimitrov, S. Frauendorf, and F. Dönau, *Phys. Rev. Lett.* **84**, 5732 (2000).
- [21] P. Olbratowski, J. Dobaczewski, J. Dudek, and W. Plóciennik, *Phys. Rev. Lett.* **93**, 052501 (2004).
- [22] P. Olbratowski, J. Dobaczewski, and J. Dudek, *Phys. Rev. C* **73**, 054308 (2006).
- [23] P. W. Zhao, *Phys. Lett. B* **773**, 1 (2017).
- [24] J. Meng, J. Peng, S. Q. Zhang, and S.-G. Zhou, *Phys. Rev. C* **73**, 037303 (2006).
- [25] A. D. Ayangeakaa, U. Garg, M. D. Anthony, S. Frauendorf, J. T. Matta, B. K. Nayak, D. Patel, Q. B. Chen, S. Q. Zhang, P. W. Zhao, et al., *Phys. Rev. Lett.* **110**, 172504 (2013).
- [26] S. Zhu, U. Garg, B. K. Nayak, S. S. Ghugre, N. S. Pattabiraman, D. B. Fossan, T. Koike, K. Starosta, C. Vaman, R. V. F. Janssens, et al., *Phys. Rev. Lett.* **91**, 132501 (2003).
- [27] S. Mukhopadhyay, D. Almeded, U. Garg, S. Frauendorf, T. Li, P. V. M. Rao, X. Wang, S. S. Ghugre, M. P. Carpenter, S. Gros, et al., *Phys. Rev. Lett.* **99**, 172501 (2007).
- [28] B. F. Lv, C. M. Petrache, Q. B. Chen, J. Meng, A. Astier, E. Dupont, P. Greenlees, H. Badran, T. Calverley, D. M. Cox, et al., *Phys. Rev. C* **100**, 024314 (2019).
- [29] P. W. Zhao, S. Q. Zhang, and J. Meng, *Phys. Rev. C* **92**, 034319 (2015).
- [30] S. Brant and C. M. Petrache, *Phys. Rev. C* **79**, 054326 (2009).
- [31] P.-G. Reinhard, *Rep. Prog. Phys.* **52**, 439 (1989).
- [32] P. Ring, *Prog. Part. Nucl. Phys.* **37**, 193 (1996).
- [33] B. Serot and J. D. Walecka, *Int. J. Mod. Phys. E* **6**, 515 (1997).
- [34] D. Vretenar, A. V. Afanasjev, G. A. Lalazissis, and P. Ring, *Phys. Rep.* **409**, 101 (2005).
- [35] J. Meng, H. Toki, S. Zhou, S. Zhang, W. Long, and L. Geng, *Prog. Part. Nucl. Phys.* **57**, 470 (2006).
- [36] J. König and P. Ring, *Phys. Rev. Lett.* **71**, 3079 (1993).
- [37] H. Madokoro, J. Meng, M. Matsuzaki, and S. Yamaji, *Phys. Rev. C* **62**, 061301 (2000).
- [38] J. Peng, J. Meng, P. Ring, and S. Q. Zhang, *Phys. Rev. C* **78**, 024313 (2008).
- [39] P. W. Zhao, S. Q. Zhang, J. Peng, H. Z. Liang, P. Ring, and J. Meng, *Phys. Lett. B* **699**, 181 (2011).
- [40] D. Steppenbeck, R. V. F. Janssens, S. J. Freeman, M. P. Carpenter, P. Chowdhury, A. N. Deacon, M. Honma, H. Jin, T. Lauritsen, C. J. Lister, et al., *Phys. Rev. C* **85**, 044316 (2012).
- [41] L. F. Yu, P. W. Zhao, S. Q. Zhang, P. Ring, and J. Meng, *Phys. Rev. C* **85**, 024318 (2012).
- [42] P. W. Zhao, J. Peng, H. Z. Liang, P. Ring, and J. Meng, *Phys. Rev. Lett.* **107**, 122501 (2011).
- [43] P. W. Zhao, J. Peng, H. Z. Liang, P. Ring, and J. Meng, *Phys. Rev. C* **85**, 054310 (2012).
- [44] P. Zhang, B. Qi, and S. Y. Wang, *Phys. Rev. C* **89**, 047302 (2014).
- [45] J. Peng and P. W. Zhao, *Phys. Rev. C* **91**, 044329 (2015).
- [46] J. Peng, H. Sagawa, S. Q. Zhang, J. M. Yao, Y. Zhang, and J. Meng, *Phys. Rev. C* **77**, 024309 (2008).

- [47] J. M. Yao, B. Qi, S. Q. Zhang, J. Peng, S. Y. Wang, and J. Meng, Phys. Rev. C **79**, 067302 (2009).
- [48] J. Li, S. Q. Zhang, and J. Meng, Phys. Rev. C **83**, 037301 (2011).
- [49] J. Li, Phys. Rev. C **97**, 034306 (2018).
- [50] B. Qi, H. Jia, C. Liu, and S. Y. Wang, Phys. Rev. C **98**, 014305 (2018).
- [51] J. Peng and Q. B. Chen, Phys. Rev. C **98**, 024320 (2018).
- [52] C. M. Petrache, B. F. Lv, A. Astier, E. Dupont, Y. K. Wang, S. Q. Zhang, P. W. Zhao, Z. X. Ren, J. Meng, P. T. Greenlees, et al., Phys. Rev. C **97**, 041304(R) (2018).
- [53] P. W. Zhao, Y. K. Wang, and Q. B. Chen, Phys. Rev. C **99**, 054319 (2019).
- [54] P. W. Zhao, Z. P. Li, J. M. Yao, and J. Meng, Phys. Rev. C **82**, 054319 (2010).
- [55] Q. B. Chen, S. Q. Zhang, P. W. Zhao, R. V. Jolos, and J. Meng, Phys. Rev. C **87**, 024314 (2013).
- [56] D. Almeded, F. Dönau, and S. Frauendorf, Phys. Rev. C **83**, 054308 (2011).
- [57] Q. B. Chen, S. Q. Zhang, P. W. Zhao, R. V. Jolos, and J. Meng, Phys. Rev. C **94**, 044301 (2016).
- [58] J. Meng, Acta Physica Sinica **42**, 368 (1993).
- [59] S. Frauendorf and J. Meng, Z. Phys. A **356**, 263 (1996).
- [60] J. M. Allmond and J. L. Wood, Phys. Lett. B **767**, 226 (2017).
- [61] See e.g., <https://www.sciencemag.org/news/2001/02/nuclei-crash-through-looking-glass>.